Available online at www.sciencedirect.com
SCIENCE DIRECT®
ELSEVIER
International Journal of Solids and Structures 43 (2006) 5468–5484
INTERNATIONAL JOURNAL OF SOLIDS and STRUCTURES
www.elsevier.com/locate/ijsolstr

Finite element analysis of smart functionally graded plates

M.C. Ray *, H.M. Sachade

Indian Institute of Technology, Kharagpur 721 302, India

Received 27 April 2005; received in revised form 30 June 2005
Available online 5 October 2005

Abstract

This paper deals with the derivation of a finite element model for the static analysis of functionally graded (FG) plates integrated with a layer of piezoelectric fiber reinforced composite (PFRC) material. The layer of PFRC material acts as the distributed actuator of the FG plates. The Young's modulus of the FG plate is assumed to vary exponentially along the thickness of the plate while the Poisson's ratio is assumed to be constant over the domain of the plate. The finite element model has been verified with the exact solutions for both thick and thin plates. Emphasis has been placed on investigating the effect of variation of piezoelectric fiber angle in the PFRC layer on its actuating capability of the FG plates. The finite element solutions also revealed that the activated PFRC layer is more effective in controlling the deformations of the FG plates when the layer is attached to the surface of the FG plate with minimum stiffness than when it is attached to the surface of the same with maximum stiffness.
© 2005 Elsevier Ltd. All rights reserved.

Keywords: Functionally graded; Smart structures; Piezo-composite; Finite element; Distributed actuator

1. Introduction

Recently, functionally graded materials (FGM) have been emerged as the new class of materials which exhibit smooth variation of material properties particularly across the thickness direction. In an endeavor to develop the super heat resistant materials for using in space plane, Koizumi (1993) first proposed the concept of FGM. The laminated composite structures can be tailored to design advanced structures with high stiffness to weight ratios, high strength to weight ratios and better thermal and transport properties. However, the sharp change in properties of each layer at the interface between the two adjacent layers of laminated composite structures causes large interlaminar shear stresses which eventually may give rise to initiation of delamination. Such detrimental effect can be circumvented if the properties smoothly vary

* Corresponding author.
E-mail address: mcray@mech.iitkgp.ernet.in (M.C. Ray).

0020-7683/$ - see front matter © 2005 Elsevier Ltd. All rights reserved.
doi:10.1016/j.ijsolstr.2005.06.096

across the thickness direction and thus the use of FGM may become an important issue for advanced structural applications. A general introduction to these FGMs encompassing the fabrication, characterization and design of these materials has been presented by Suresh and Mortensen (1998). During the past few years a large number of researches have been reported to analyze the behavior of functionally graded materials. For example, Teymur et al. (1996) carried out the thermomechanical analysis of materials which are functionally graded in two directions and demonstrated that the onset of delamination could be prevented by tailoring the microstructures of the composite plies. Feldman and Aboudi (1997) studied the elastic bifurcational buckling of functionally graded plates under in-plane compressive load. They concluded that with optimal nonuniform distribution of reinforcing phases, the buckling load can be significantly improved for FG plate over the plate with uniformly distributed reinforcing phase. Mian and Spencer (1998) derived the exact solutions for functionally graded plates with zero surface traction. Gasik (1998) developed an efficient micromechanical model for FGMs with an arbitrary non-linear 3D-distribution of phases. This model has been reported to provide accurate estimates of the properties of the FGMs. The model is also capable of computing thermal stresses, evaluating dynamic stress/strain distribution and inelastic behavior of FGMs. Praveen and Reddy (1998) investigated the nonlinear thermoelastic behavior of functionally graded ceramic metal plates. Loy et al. (1999) studied the vibration of cylindrical shells made of a functionally graded material which is composed of stainless steel and nickel. Aboudi et al. (1999) further developed a more general higher-order theory for functionally graded materials and illustrated the utility of functionally graded microstructures in tailoring the behavior of structural components in various applications. In 2000, Wang et al. (2000) proposed a method to determine the transient and steady state thermal stress intensity factors of graded composite plate containing noncollinear cracks subjected to dynamic thermal loading. Yang (2000) presented an analytical solution for computing the time-dependent stresses in FGM undergoing creep. Yang and Shen (2001) studied the dynamic response of initially stressed functionally graded thin plates subjected to partially distributed impulsive loads. An elasticity solution for functionally graded beams is provided by Sankar (2001) in which the beam properties are graded in the thickness direction according to an exponential law. The exact solutions for thermoelastic deformations of thick FG plates subjected to both thermal and mechanical loads have been presented by Batra and Vel (2001). Woo and Meguid (2001) presented an analytical solution for the large deflections of plates and shallow shells made of FGMs under the combined action of thermal and mechanical loads. Reddy and Cheng (2001) presented the three dimensional solutions for functionally graded plates coupled with piezoelectric actuator layer employing transfer matrix and asymptotic expansion techniques. Shen (2002) also carried out nonlinear bending analysis for simply supported functionally graded plate subjected to mechanical and thermal loadings using a higher-order shear deformation theory. Considering time-dependent thermal loads, Vel and Batra (2003) presented an analytical solution for three-dimensional thermomechanical deformation of a simply-supported FG plate. Yang et al. (2003) performed an analysis of prestressed functionally graded laminated plates integrated with piezoelectric actuator to predict the large amplitude vibration behavior of the plates. Chakraborty et al. (2003) developed a new beam type finite element for the analysis of functionally graded materials. Santare et al. (2003) simulated the elastic wave propagation in the functionally graded materials using graded finite elements. Chakraborty and Gopalakrishnan (2003) employed spectral finite element method to analyze the wave propagation in a functionally graded beam. More recently, Chen et al. (2004) studied the transient heat transfer analysis of functionally graded materials using adaptive precise time integration and graded finite elements.

In the quest for developing light-weight high performing flexible structures a concept was emerged to develop the structures with self-controlling and self-monitoring capabilities. Expediently, it was discovered that if the piezoelectric materials are used as distributed actuators and sensors which are either mounted on or embedded in the structure then the structure attains these self-controlling and self-monitoring capabilities (Bailey and Hubbard, 1985; Miller and Hubbard, 1987). Such structures are customarily called as "smart structures". Piezoelectric materials induce an electric potential/charge when they are subjected to

a mechanical load by virtue of the direct piezoelectric effect and are deformed due to the externally applied voltage/charge by virtue of the converse piezoelectric effect. Use of piezoelectric materials as distributed sensors and actuators for developing smart structures is attributed to these two phenomena. The concept of developing smart structures has been extensively employed for the active vibration control of flexible structures during the past decade (Crawley and Luis, 1987; Baz and Poh, 1988; Ray et al., 1993; Baz and Poh, 1996; Stöbener and Gaul, 2000; Dong and Tong, 2001; Ray, 2003; Ray and Reddy, 2004). However, the main drawback of the existing monolithic piezoelectric materials which are being used in smart structures is that the control authority of these materials is very low as their piezoelectric stress/strain co-efficients are of very small magnitudes. As the active damping of smart structures depends on the control authority of the piezoelectric materials, tailoring of the piezoelectric stress/strain coefficients may improve their control authority and hence the damping characteristics of lightweight smart structures can be improved. In an endeavor to tailor the piezoelectric properties, Mallik and Ray (2003) newly proposed the concept of longitudinally piezoelectric fiber reinforced composite (PFRC) materials and investigated the effective mechanical and piezoelectric properties of these composites. The main concern of the investigations was to determine the effective piezoelectric co-efficient ($\mathbf{e}_{31}$) of these new concept PFRC materials which quantifies the induced normal stress in the fiber direction due to the applied electric field in the direction transverse to the fiber direction. They predicted that this effective piezoelectric co-efficient becomes significantly larger than the corresponding co-efficient of piezoelectric material of the fibers. Note that the measure of active control of flexural vibration of smart structures depends mainly on the magnitude of this piezoelectric co-efficient.

In an attempt towards the development of new functionally graded smart structures, authors first derived the exact solutions (Ray and Sachade, accepted for publication) for the simply supported functionally graded plates integrated with the layer of the new piezoelectric fiber reinforced composite (PFRC) material as mentioned above. However, it is well known that the exact solutions for the problems with more general boundary conditions subjected to arbitrary loading can not be derived and the finite element method has been firmly established as a most popular tool for solving such problems. Although, the literature review indicates that the plenty of work has been done on the theoretical analysis of functionally graded structures, only handful amount of work (Chakraborty et al., 2003; Santare et al., 2003; Chakraborty and Gopalakrishnan, 2003; Chen et al., 2004) have been reported towards the development of finite element model of functionally graded structures. In this paper, authors intend to present a finite element model of functionally graded (FG) plates integrated with a layer of the piezoelectric fiber reinforced composite (PFRC) material which acts as the distributed actuator of the plates. The model has been verified with the exact solutions. The performance of the activated PFRC layer due to the variation of the piezoelectric fiber angle has also been studied using this finite element model.

2. Finite element modeling

Fig. 1 shows a simply supported rectangular functionally graded (FG) plate. The top surface of the plate is integrated with a layer of the piezoelectric fiber reinforced composite (PFRC) material, acting as a distributed actuator of the FG plate. When the PFRC layer is subjected to externally applied voltage according to an appropriate control strategy, the overall plate turns out to be a smart functionally graded plate. The length, width and thickness of the plate are denoted by $\mathbf{a}$, $\mathbf{b}$ and $\mathbf{h}$, respectively and the thickness of the PFRC layer is denoted by $\mathbf{h}_p$. The constructional feature of the lamina made of this PFRC material has been schematically illustrated elsewhere (Mallik and Ray, 2003). The mid plane of the substrate plate is considered as the reference plane. The origin of the reference Cartesian co-ordinate system $(\mathbf{x}, \mathbf{y}, \mathbf{z})$ is located on the reference plane in such a way that the lines $\mathbf{x} = 0,\mathbf{a}$ and $\mathbf{y} = 0,\mathbf{b}$ represent the boundaries of the overall plate. The fibers in the PFRC layer are horizontally reinforced and are oriented at an angle ψ with respect to the reference coordinate system.

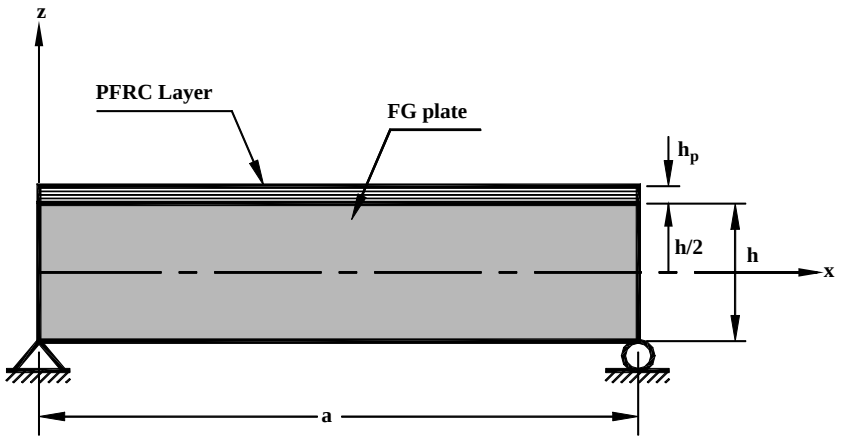

Fig. 1. Schematic diagram of a smart functionally graded plate.

The kinematics of deformations of the overall plate is considered to be based on the first order shear deformation theory (FSDT). According to this theory, the displacements **u**, **v** and **w** at any point in the overall plate along, **x**, **y** and **z** directions, respectively are given by

$$\mathbf{u}(\mathbf{x},\mathbf{y},\mathbf{z}) = \mathbf{u}_0(\mathbf{x},\mathbf{y}) + \mathbf{z}\boldsymbol{\theta}_\mathbf{x}(\mathbf{x},\mathbf{y}) \tag{1}$$

$$\mathbf{v}(\mathbf{x},\mathbf{y},\mathbf{z}) = \mathbf{v}_0(\mathbf{x},\mathbf{y}) + \mathbf{z}\boldsymbol{\theta}_\mathbf{y}(\mathbf{x},\mathbf{y}) \tag{2}$$

$$\mathbf{w}(\mathbf{x},\mathbf{y},\mathbf{z}) = \mathbf{w}_0(\mathbf{x},\mathbf{y}) \tag{3}$$

in which $\mathbf{u}_0$, $\mathbf{v}_0$, $\mathbf{w}_0$ are the generalized displacements of a reference point $(\mathbf{x},\mathbf{y})$ on the mid-plane $(\mathbf{z}=0)$ of the substrate FG plate along **x**, **y** and **z** axes, respectively; $\boldsymbol{\theta}_\mathbf{x}$ and $\boldsymbol{\theta}_\mathbf{y}$ are the generalized rotations of the normal to reference point on the reference plane $(\mathbf{z}=0)$ lying in the **xz** and **yz** planes, respectively. For the ease of analysis, the generalized displacement variables are separated into translational $\{\mathbf{d}_t\}$ and rotational $\{\mathbf{d}_r\}$ variables as follows:

$$\{\mathbf{d}_t\} = [\,\mathbf{u}_0 \quad \mathbf{v}_0 \quad \mathbf{w}_0\,]^T \quad \text{and} \quad \{\mathbf{d}_r\} = [\,\boldsymbol{\theta}_\mathbf{x} \quad \boldsymbol{\theta}_\mathbf{y}\,]^T \tag{4}$$

The state of strains at any point in the overall plate is described by the in-plane strains $\{\boldsymbol{\epsilon}_b\}$ and transverse shear strains $\{\boldsymbol{\epsilon}_s\}$ as follows:

$$\{\boldsymbol{\epsilon}_b\} = [\,\boldsymbol{\epsilon}_\mathbf{x} \quad \boldsymbol{\epsilon}_\mathbf{y} \quad \boldsymbol{\epsilon}_\mathbf{xy}\,]^T \quad \text{and} \quad \{\boldsymbol{\epsilon}_s\} = [\,\boldsymbol{\epsilon}_\mathbf{xz} \quad \boldsymbol{\epsilon}_\mathbf{yz}\,]^T \tag{5}$$

in which $\boldsymbol{\epsilon}_\mathbf{x}$, $\boldsymbol{\epsilon}_\mathbf{y}$ are the normal strain along **x** and **y** directions, respectively, $\boldsymbol{\epsilon}_\mathbf{xy}$ is the in-plane shear strain and $\boldsymbol{\epsilon}_\mathbf{xz}$,$\boldsymbol{\epsilon}_\mathbf{yz}$ are the transverse shear strains. Using the linear strain–displacement relations and the displacement field given by Eqs. (1)–(3), the in-plane strain vector $\{\boldsymbol{\epsilon}_b\}$ and the transverse shear strain vector $\{\boldsymbol{\epsilon}_s\}$ can be expressed as

$$\{\boldsymbol{\epsilon}_b\} = \{\boldsymbol{\epsilon}_{bt}\} + \mathbf{z}\{\boldsymbol{\epsilon}_{br}\} \quad \text{and} \quad \{\boldsymbol{\epsilon}_s\} = \{\boldsymbol{\epsilon}_{st}\} + \{\boldsymbol{\epsilon}_{sr}\} \tag{6}$$

where the generalized strain vectors $\{\boldsymbol{\epsilon}_{bt}\}$, $\{\boldsymbol{\epsilon}_{br}\}$, $\{\boldsymbol{\epsilon}_{st}\}$ and $\{\boldsymbol{\epsilon}_{sr}\}$ are given by

$$\begin{aligned}
\{\boldsymbol{\epsilon}_{bt}\} &= \left[\frac{\partial \mathbf{u}_0}{\partial \mathbf{x}} \quad \frac{\partial \mathbf{v}_0}{\partial \mathbf{y}} \quad \frac{\partial \mathbf{u}_0}{\partial \mathbf{y}} + \frac{\partial \mathbf{v}_0}{\partial \mathbf{x}}\right]^T, \quad \{\boldsymbol{\epsilon}_{br}\} = \left[\frac{\partial \boldsymbol{\theta}_\mathbf{x}}{\partial \mathbf{x}} \quad \frac{\partial \boldsymbol{\theta}_\mathbf{y}}{\partial \mathbf{y}} \quad \frac{\partial \boldsymbol{\theta}_\mathbf{x}}{\partial \mathbf{y}} + \frac{\partial \boldsymbol{\theta}_\mathbf{y}}{\partial \mathbf{x}}\right]^T, \\
\{\boldsymbol{\epsilon}_{st}\} &= \left[\frac{\partial \mathbf{w}_0}{\partial \mathbf{x}} \quad \frac{\partial \mathbf{w}_0}{\partial \mathbf{y}}\right]^T \quad \text{and} \quad \{\boldsymbol{\epsilon}_{sr}\} = [\,\boldsymbol{\theta}_\mathbf{x} \quad \boldsymbol{\theta}_\mathbf{y}\,]^T
\end{aligned} \tag{7}$$

It is assumed that the surface of the PFRC layer being in contact with the substrate FG plate is suitably grounded. Since, the thickness of the PFRC layer is very small, the variation of the electric potential function across the thickness may be considered as linear. Thus the form of the electric potential function $\boldsymbol{\phi}(\mathbf{x},\mathbf{y},\mathbf{z})$ in the PFRC layer can be expressed as

$$\begin{aligned}\text{either}\quad & \boldsymbol{\phi}(\mathbf{x},\mathbf{y},\mathbf{z}) = (\mathbf{z}-\mathbf{h}/\mathbf{2})\boldsymbol{\phi}_0(\mathbf{x},\mathbf{y})/\mathbf{h}_\mathrm{p}, \mathbf{h}/2 \leqslant \mathbf{z} \leqslant \mathbf{h}/2+\mathbf{h}_\mathrm{p} \quad \text{or}\\ & \boldsymbol{\phi}(\mathbf{x},\mathbf{y},\mathbf{z}) = -(\mathbf{z}+\mathbf{h}/2)\boldsymbol{\phi}_0(\mathbf{x},\mathbf{y})/\mathbf{h}_\mathrm{p}, -(\mathbf{h}/\mathbf{2}+\mathbf{h}_\mathrm{p}) \leqslant \mathbf{z} \leqslant -\mathbf{h}/2\end{aligned} \tag{8}$$

according as the top or bottom surface of the FG plate is integrated with the PFRC layer. In the expression for $\boldsymbol{\phi}$ given by (8), $\boldsymbol{\phi}_0$ is the generalized electric potential function similar to the generalized displacement functions at any point on the top or bottom surface of the PFRC layer.

Similar to the strain vectors given by Eq. (5), the inplane stresses and transverse shear stresses at any point in the overall plate are described by the following stress vectors

$$\{\boldsymbol{\sigma}_\mathrm{b}^k\} = \left[\begin{array}{ccc}\boldsymbol{\sigma}_\mathbf{x}^k & \boldsymbol{\sigma}_y^k & \boldsymbol{\sigma}_\mathbf{xy}^k\end{array}\right]^\mathrm{T} \quad \text{and} \quad \{\boldsymbol{\sigma}_\mathrm{s}^k\} = \left[\begin{array}{cc}\boldsymbol{\sigma}_\mathrm{xz}^k & \boldsymbol{\sigma}_\mathrm{yz}^k\end{array}\right]^\mathrm{T}, \quad k = 1 \text{ and } 2 \tag{9}$$

where, $\boldsymbol{\sigma}_\mathbf{x}$ and $\boldsymbol{\sigma}_\mathbf{y}$ are the normal stresses along $\mathbf{x}$ and $\mathbf{y}$ directions, respectively; $\boldsymbol{\sigma}_\mathbf{xy}$ is the inplane shear stress; $\boldsymbol{\sigma}_\mathbf{xz}$ and $\boldsymbol{\sigma}_\mathbf{yz}$ are the transverse shear stresses. In the formulation, the value of the superscript k identify either the substrate FG plate or the PFRC layer according as the top or bottom surface of the FG plate is integrated with the PFRC layer. For example, if the top surface of the FG plate is integrated with the PFRC layer then the values of k as 1 and 2 denote the FG plate and the PFRC layer, respectively and vice versa. The constitutive relations for the material of the elastic FG plate are given by Sankar (2001)

$$\{\boldsymbol{\sigma}_\mathrm{b}^k\} = [\overline{\mathbf{C}}_\mathrm{b}^k]\{\boldsymbol{\epsilon}_\mathrm{b}\} \quad \text{and} \quad \{\boldsymbol{\sigma}_\mathrm{s}^k\} = [\overline{\mathbf{C}}_\mathrm{s}^k]\{\boldsymbol{\epsilon}_\mathrm{s}\} \tag{10}$$

In general, the stress tensor in the PFRC material is not symmetric due to the electro-mechanical coupling. However, as the stress due to this coupling is very small compared to the purely mechanical stress, it may be neglected and the resulting stress tensor becomes symmetric. Thus, the constitutive relations for the material of the PFRC layer are given by Mallik and Ray (2003)

$$\{\boldsymbol{\sigma}_\mathrm{b}^k\} = [\overline{\mathbf{C}}_\mathrm{b}^k]\{\boldsymbol{\epsilon}_\mathrm{b}\} - [\bar{\mathbf{e}}_\mathrm{b}]\{\mathbf{E}\} \quad \text{and} \quad \{\boldsymbol{\sigma}_\mathrm{s}^k\} = [\overline{\mathbf{C}}_\mathrm{s}^k]\{\boldsymbol{\epsilon}_s\} - [\bar{\mathbf{e}}_s]\{\mathbf{E}\}, \tag{11}$$

$$\{\mathbf{D}\} = [\bar{\mathbf{e}}_\mathrm{b}]^\mathrm{T}\{\boldsymbol{\epsilon}_\mathrm{b}^k\} + [\bar{\mathbf{e}}_\mathrm{s}^k]^\mathrm{T}\{\boldsymbol{\epsilon}_\mathrm{s}^k\} + [\bar{\boldsymbol{\epsilon}}]\{\mathbf{E}^k\} \tag{12}$$

In Eqs. (10)–(12), $[\overline{\mathbf{C}}_\mathrm{b}^k]$ and $[\overline{\mathbf{C}}_\mathrm{s}^k]$ are the matrices of transformed elastic coefficients referred to reference $(\mathbf{x},\mathbf{y},\mathbf{z})$ coordinate systems; The transformed piezoelectric coefficient matrices $[\bar{\mathbf{e}}_\mathrm{b}]$ and $[\bar{\mathbf{e}}_\mathrm{s}]$ and the dielectric constant matrix $[\bar{\boldsymbol{\epsilon}}]$ of the PFRC layer are given by

$$[\bar{\mathbf{e}}_\mathrm{b}] = \begin{bmatrix}0 & 0 & \bar{\mathbf{e}}_{31}\\ 0 & 0 & \bar{\mathbf{e}}_{32}\\ 0 & 0 & \bar{\mathbf{e}}_{36}\end{bmatrix}, \quad [\bar{\mathbf{e}}_s] = \begin{bmatrix}\bar{\mathbf{e}}_{15} & \bar{\mathbf{e}}_{25} & 0\\ \bar{\mathbf{e}}_{14} & \bar{\mathbf{e}}_{24} & 0\end{bmatrix} \quad \text{and} \quad [\bar{\boldsymbol{\epsilon}}] = \begin{bmatrix}\bar{\boldsymbol{\epsilon}}_{11} & \bar{\boldsymbol{\epsilon}}_{12} & 0\\ \bar{\boldsymbol{\epsilon}}_{12} & \bar{\boldsymbol{\epsilon}}_{22} & 0\\ 0 & 0 & \bar{\boldsymbol{\epsilon}}_{33}\end{bmatrix} \tag{13}$$

Also, the electric field vector $\{\mathbf{E}\}$ and the electric displacement vector $\{\mathbf{D}\}$ appearing in Eqs. (11) and (12) are given by

$$\{\mathbf{E}\} = \left[\begin{array}{ccc}\mathbf{E}_\mathbf{x} & \mathbf{E}_y & \mathbf{E}_\mathrm{z}\end{array}\right]^\mathrm{T} \quad \text{and} \quad \{\mathbf{D}\} = \left[\begin{array}{ccc}\mathbf{D}_\mathbf{x} & \mathbf{D}_y & \mathbf{D}_\mathrm{z}\end{array}\right]^\mathrm{T} \tag{14}$$

in which, $\mathbf{E}_\mathbf{x}$, $\mathbf{E}_\mathbf{y}$ and $\mathbf{E}_\mathbf{z}$ are the electric fields along the $\mathbf{x}$, $\mathbf{y}$ and $\mathbf{z}$ directions, respectively and $\mathbf{D}_\mathbf{x}$, $\mathbf{D}_\mathbf{y}$ and $\mathbf{D}_\mathbf{z}$ are the corresponding electric displacements.

It is assumed that the FG material considered in this study is isotropic at any point but its Young's modulus $\mathbf{E}$ is an exponential function of $\mathbf{z}$ (Sankar, 2001) and is given by

$$\mathbf{E} = \mathbf{E}_0 \mathrm{e}^{\lambda(\mathbf{z}+\mathbf{h}/2)} \tag{15}$$

where $\mathbf{E}_0$ refers to the Young's modulus of the material located at the bottom surface of the FG plate and $\boldsymbol{\lambda}$ is a parameter describing the inhomogeneity of the FG material across the thickness. It is also assumed that the Poisson's ratio is constant over the domain of the FG plate. Thus the elastic coefficients of the material of the FG plate are given by

$$[\overline{\mathbf{C}}_{\mathrm{b}}^{1}] = [\overline{\mathbf{C}}_{\mathrm{b}}^{0}]\mathrm{e}^{\boldsymbol{\lambda}(\mathbf{z}+\mathbf{h}/2)} \quad \text{and} \quad [\overline{\mathbf{C}}_{\mathrm{s}}^{1}] = [\overline{\mathbf{C}}_{\mathrm{s}}^{0}]\mathrm{e}^{\boldsymbol{\lambda}(\mathbf{z}+\mathbf{h}/2)} \tag{16}$$

in which $[\overline{\mathbf{C}}_{\mathrm{b}}^{0}]$ and $[\overline{\mathbf{C}}_{\mathrm{s}}^{0}]$ are the elastic coefficient matrices for the isotropic material located at the bottom surface of the FG plate relating the in-plane strains to the in-plane stresses and transverse shear strains to transverse shear stresses, respectively.

The total potential energy of the FG plate coupled with the PFRC layer is given by

$$\mathbf{T}_{\mathrm{P}} = \frac{1}{2}\left[\sum_{k=1}^{2}\int_{\mathfrak{V}}(\{\boldsymbol{\epsilon}_{\mathrm{b}}^{k}\}^{\mathrm{T}}\{\boldsymbol{\sigma}_{\mathrm{b}}^{k}\} + \{\boldsymbol{\epsilon}_{\mathrm{s}}^{k}\}^{\mathrm{T}}\{\boldsymbol{\sigma}_{\mathrm{s}}^{k}\})\mathrm{d}\mathfrak{V} - \int_{\mathfrak{V}}\{\mathbf{E}\}^{\mathrm{T}}\{\mathbf{D}\}d\mathfrak{V}\right] - \int_{\mathrm{A}}\{\mathbf{d}\}^{\mathrm{T}}\{\mathbf{f}\}\mathrm{d}\mathbf{A} \tag{17}$$

where, $\{\mathbf{f}\}$ is the externally applied surface traction vector acting over a surface area $\mathbf{A}$ and $\mathfrak{V}$ represents the volume of the concerned domain.

Eight noded isoparametric quadrilateral elements have been considered for discretizing the overall plate. Thus using Eq. (4), the generalized displacement vectors for the ith ($i = 1, 2, 3, \ldots, 8$) node of the element can be denoted as

$$\{\mathbf{d}_{\mathrm{ti}}\} = [\,\mathbf{u}_{0i} \quad \mathbf{v}_{0i} \quad \mathbf{w}_{0i}\,]^{\mathrm{T}} \quad \text{and} \quad \{\mathbf{d}_{\mathrm{ri}}\} = [\,\boldsymbol{\theta}_{\mathrm{xi}} \quad \boldsymbol{\theta}_{\mathrm{yi}}\,]^{\mathrm{T}} \tag{18}$$

and subsequently, the generalized displacement vectors at any point within the element can be written as:

$$\{\mathbf{d}_{\mathrm{t}}\} = [\mathbf{N}_{\mathrm{t}}]\{\mathbf{d}_{\mathrm{t}}^{\mathrm{e}}\} \quad \text{and} \quad \{\mathbf{d}_{\mathrm{r}}\} = [\mathbf{N}_{\mathrm{r}}]\{\mathbf{d}_{\mathrm{r}}^{\mathrm{e}}\} \tag{19}$$

In Eq. (19), the nodal generalized translational displacement vector $\{\mathbf{d}_{\mathrm{t}}^{\mathrm{e}}\}$, the nodal generalized rotational displacement vector $\{\mathbf{d}_{\mathrm{r}}^{\mathrm{e}}\}$ and the shape function matrices $[\mathbf{N}_{\mathrm{t}}]$ and $[\mathbf{N}_{\mathrm{r}}]$ are given by

$$\begin{aligned} &\{\mathbf{d}_{\mathrm{t}}^{\mathrm{e}}\} = \left[\,\{\mathbf{d}_{\mathrm{t1}}\}^{\mathrm{T}} \quad \{\mathbf{d}_{\mathrm{t2}}\}^{\mathrm{T}} \quad \ldots \quad \{\mathbf{d}_{\mathrm{t8}}\}^{\mathrm{T}}\,\right]^{\mathrm{T}}, \quad \{\mathbf{d}_{\mathrm{r}}^{\mathrm{e}}\} = \left[\,\{\mathbf{d}_{\mathrm{r1}}\}^{\mathrm{T}} \quad \{\mathbf{d}_{\mathrm{r2}}\}^{\mathrm{T}} \quad \ldots \quad \{\mathbf{d}_{\mathrm{r8}}\}^{\mathrm{T}}\,\right]^{\mathrm{T}}, \\ &[\mathbf{N}_{\mathrm{t}}] = [\,\mathbf{N}_{\mathrm{t1}} \quad \mathbf{N}_{\mathrm{t2}} \quad \ldots \quad \mathbf{N}_{\mathrm{t8}}\,], \quad [\mathbf{N}_{\mathrm{r}}] = [\,\mathbf{N}_{\mathrm{r1}} \quad \mathbf{N}_{\mathrm{r2}} \quad \ldots \quad \mathbf{N}_{\mathrm{r8}}\,], \quad \mathbf{N}_{\mathrm{t}i} = \mathbf{n}_i\mathbf{I}_{\mathrm{t}} \quad \text{and} \quad \mathbf{N}_{\mathrm{r}i} = \mathbf{n}_i\mathbf{I}_{\mathrm{r}} \end{aligned} \tag{20}$$

wherein, $\mathbf{I}_{\mathrm{t}}$ and $\mathbf{I}_{\mathrm{r}}$ are the identity matrices and $\mathbf{n}_i$ is the shape function of natural coordinates associated with the node i. Using the relations given by Eqs. (6), (7) and (19), the generalized strain vectors at any point within the element can be expressed as

$$\{\boldsymbol{\epsilon}_{\mathrm{b}}\} = [\mathbf{B}_{\mathrm{tb}}]\{\mathbf{d}_{\mathrm{t}}^{\mathrm{e}}\} + \mathbf{z}[\mathbf{B}_{\mathrm{rb}}]\{\mathbf{d}_{\mathrm{r}}^{\mathrm{e}}\} \quad \text{and} \quad \{\boldsymbol{\epsilon}_{\mathrm{s}}\} = [\mathbf{B}_{\mathrm{ts}}]\{\mathbf{d}_{\mathrm{t}}^{\mathrm{e}}\} + [\mathbf{B}_{\mathrm{rs}}]\{\mathbf{d}_{\mathrm{r}}^{\mathrm{e}}\} \tag{21}$$

In Eq. (21), the nodal generalized strain–displacement matrices $[\mathbf{B}_{\mathrm{tb}}]$, $[\mathbf{B}_{\mathrm{rb}}]$, $[\mathbf{B}_{\mathrm{ts}}]$ and $[\mathbf{B}_{\mathrm{rs}}]$ are given by

$$\begin{aligned} &[\mathbf{B}_{\mathrm{tb}}] = [\,\mathbf{B}_{\mathrm{tb1}} \quad \mathbf{B}_{\mathrm{tb2}} \quad \ldots \quad \mathbf{B}_{\mathrm{tb8}}\,], \quad [\mathbf{B}_{\mathrm{rb}}] = [\,\mathbf{B}_{\mathrm{rb1}} \quad \mathbf{B}_{\mathrm{rb2}} \quad \ldots \quad \mathbf{B}_{\mathrm{rb8}}\,], \\ &[\mathbf{B}_{\mathrm{ts}}] = [\,\mathbf{B}_{\mathrm{ts1}} \quad \mathbf{B}_{\mathrm{ts2}} \quad \ldots \quad \mathbf{B}_{\mathrm{ts8}}\,] \quad \text{and} \quad [\mathbf{B}_{\mathrm{rs}}] = [\,\mathbf{B}_{\mathrm{rs1}} \quad \mathbf{B}_{\mathrm{rs2}} \quad \ldots \quad \mathbf{B}_{\mathrm{rs8}}\,] \end{aligned} \tag{22}$$

The various sub matrices appearing in (22) are given by

$$[\mathbf{B}_{\mathrm{tbi}}] = \begin{bmatrix} \dfrac{\partial \mathbf{n}_i}{\partial \mathbf{x}} & 0 & 0 \\ 0 & \dfrac{\partial \mathbf{n}_i}{\partial \mathbf{y}} & 0 \\ \dfrac{\partial \mathbf{n}_i}{\partial \mathbf{y}} & \dfrac{\partial \mathbf{n}_i}{\partial \mathbf{x}} & 0 \end{bmatrix}, \quad [\mathbf{B}_{\mathrm{rbi}}] = \begin{bmatrix} \dfrac{\partial \mathbf{n}_i}{\partial \mathbf{x}} & 0 \\ 0 & \dfrac{\partial \mathbf{n}_i}{\partial \mathbf{y}} \\ \dfrac{\partial \mathbf{n}_i}{\partial \mathbf{y}} & \dfrac{\partial \mathbf{n}_i}{\partial \mathbf{x}} \end{bmatrix}, \quad [\mathbf{B}_{\mathrm{tsi}}] = \begin{bmatrix} 0 & 0 & \dfrac{\partial \mathbf{n}_i}{\partial \mathbf{x}} \\ 0 & 0 & \dfrac{\partial \mathbf{n}_i}{\partial \mathbf{y}} \end{bmatrix}, \quad [\mathbf{B}_{\mathrm{rsi}}] = \begin{bmatrix} \mathbf{n}_i & 0 \\ 0 & \mathbf{n}_i \end{bmatrix} \tag{23}$$

The generalized electric potential vector at any point within the element can be expressed as

$$\boldsymbol{\phi}_0 = [\mathbf{N}_{\boldsymbol{\phi}}]\{\boldsymbol{\phi}_0^{\mathrm{e}}\} \tag{24}$$

where, $\{\boldsymbol{\phi}_0^e\} = [\,\boldsymbol{\phi}_{01} \quad \boldsymbol{\phi}_{02} \quad \dots \quad \boldsymbol{\phi}_{08}\,]^T$ and $[N_\phi] = [\,\mathbf{n}_1 \quad \mathbf{n}_2 \quad \dots \quad \mathbf{n}_8\,]$. Using Eqs. (8), (14) and (24) and the electric field-potential relations, the electric field vector can be expressed in terms of the nodal generalized electric potential degrees of freedom $\{\boldsymbol{\phi}_0^e\}$ as follows:

$$\{\mathbf{E}^k\} = [\mathbf{Z}_p][\mathbf{B}_p]\{\boldsymbol{\phi}_0^e\} \tag{25}$$

in which, $[\mathbf{B}_p] = [\,\mathbf{B}_{p1} \quad \mathbf{B}_{p2} \quad \dots \quad \mathbf{B}_{p8}\,]$ with

$$[\mathbf{B}_{pi}] = \begin{bmatrix} \frac{\partial \mathbf{n}_i}{\partial \mathbf{x}} & \frac{\partial \mathbf{n}_i}{\partial \mathbf{y}} & \mathbf{n}_i \end{bmatrix}^T \quad \text{and} \quad [\mathbf{Z}_p] = \frac{(-1)^k}{\mathbf{h}_p}\begin{bmatrix} -\{\mathbf{z} - (-1)^k\mathbf{h}/2\} & 0 & 0 \\ 0 & -\{\mathbf{z} - (-1)^k\mathbf{h}/2\} & 0 \\ 0 & 0 & -1 \end{bmatrix}$$

Substituting Eqs. (10)–(12) into Eq. (17) and then using Eqs. (21) and (25), the total potential energy ($\mathbf{T}_P^e$) of a typical element of the FG plate augmented with the PFRC layer can be expressed as

$$\begin{aligned}\mathbf{T}_P^e = \frac{1}{2}[&\{\mathbf{d}_t^e\}^T[\mathbf{K}_t^e]\{\mathbf{d}_t^e\} + \{\mathbf{d}_t^e\}^T[\mathbf{K}_{tr}^e]\{\mathbf{d}_r^e\} + \{\mathbf{d}_r^e\}^T[\mathbf{K}_{rt}^e]\{\mathbf{d}_t^e\} + \{\mathbf{d}_r^e\}^T[\mathbf{K}_{rr}^e]\{\mathbf{d}_r^e\} \\ &- \{\mathbf{d}_t^e\}^T[\mathbf{F}_{tp}^e]\{\boldsymbol{\phi}_0^e\} - \{\mathbf{d}_r^e\}^T[\mathbf{F}_{rp}^e]\{\boldsymbol{\phi}_0^e\} - \{\boldsymbol{\phi}_0^e\}^T[\mathbf{F}_{pt}^e]\{\mathbf{d}_t^e\} - \{\boldsymbol{\phi}_0^e\}^T[\mathbf{F}_{pr}^e]\{\mathbf{d}_r^e\} \\ &- \{\boldsymbol{\phi}_0^e\}^T[\mathbf{K}_D^e]\{\boldsymbol{\phi}_0^e\}] - \{\mathbf{d}_t^e\}^T\{\mathbf{F}^e\}\end{aligned} \tag{26}$$

In Eq. (26), the elemental stiffness matrices $[\mathbf{K}_t^e]$, $[\mathbf{K}_{tr}^e]$, $[\mathbf{K}_{rt}^e]$ and $[\mathbf{K}_{rr}^e]$; the elemental electro-elastic coupling matrices $[\mathbf{F}_{tp}^e]$, $[\mathbf{F}_{rp}^e]$, $\mathbf{F}_{pt}^e$ and $[\mathbf{F}_{pr}^e]$; the elemental dielectric stiffness matrix $[\mathbf{K}_D^e]$ and the elemental load vector $[\mathbf{F}^e]$ are defined as follows:

$$\begin{aligned}
&[\mathbf{K}_t^e] = [\mathbf{K}_{tb}^e] + [\mathbf{K}_{ts}^e], \quad [\mathbf{K}_{tr}^e] = [\mathbf{K}_{trb}^e] + [\mathbf{K}_{trs}^e], \quad [\mathbf{K}_{rr}^e] = [\mathbf{K}_{rrb}^e] + [\mathbf{K}_{rrs}^e], \quad [\mathbf{K}_{rt}^e] = [\mathbf{K}_{tr}^e]^T, \\
&[\mathbf{K}_{tb}^e] = \int_0^{\mathbf{b}_e}\int_0^{\mathbf{a}_e}[\mathbf{B}_{tb}]^T[\mathbf{D}_{tb}][\mathbf{B}_{tb}]d\mathbf{x}\,d\mathbf{y}, \quad [\mathbf{K}_{ts}^e] = \int_0^{\mathbf{b}_e}\int_0^{\mathbf{a}_e}[\mathbf{B}_{ts}]^T[\mathbf{D}_{ts}][\mathbf{B}_{ts}]d\mathbf{x}\,d\mathbf{y}, \\
&[\mathbf{K}_{trb}^e] = \int_0^{\mathbf{b}_e}\int_0^{\mathbf{a}_e}[\mathbf{B}_{tb}]^T[\mathbf{D}_{trb}][\mathbf{B}_{rb}]d\mathbf{x}\,d\mathbf{y}, \quad [\mathbf{K}_{trs}^e] = \int_0^{\mathbf{b}_e}\int_0^{\mathbf{a}_e}[\mathbf{B}_{ts}]^T[\mathbf{D}_{trs}][\mathbf{B}_{rs}]d\mathbf{x}\,d\mathbf{y}, \\
&[\mathbf{K}_{rrb}^e] = \int_0^{\mathbf{b}_e}\int_0^{\mathbf{a}_e}[\mathbf{B}_{rb}]^T[\mathbf{D}_{rrb}][\mathbf{B}_{rb}]d\mathbf{x}\,d\mathbf{y}, \quad [\mathbf{K}_{rrs}^e] = \int_0^{\mathbf{b}_e}\int_0^{\mathbf{a}_e}[\mathbf{B}_{rs}]^T[\mathbf{D}_{rrs}][\mathbf{B}_{rs}]d\mathbf{x}\,d\mathbf{y}, \\
&[\mathbf{F}_{tp}^e] = \int_0^{\mathbf{b}_e}\int_0^{\mathbf{a}_e}[\mathbf{B}_{tb}]^T[\mathbf{D}_{tp}][\mathbf{B}_p]d\mathbf{x}\,d\mathbf{y}, \quad [\mathbf{F}_{rp}^e] = \int_0^{\mathbf{b}_e}\int_0^{\mathbf{a}_e}[\mathbf{B}_{rb}]^T[\mathbf{D}_{rp}][\mathbf{B}_p]d\mathbf{x}\,d\mathbf{y}, \quad [\mathbf{F}_{pt}^e] = [\mathbf{F}_{tp}^e]^T \\
&[\mathbf{F}_{pr}^e] = [\mathbf{F}_{rp}^e]^T, \quad [\mathbf{K}_D^e] = \int_0^{\mathbf{b}_e}\int_0^{\mathbf{a}_e}[\mathbf{B}_p]^T[\mathbf{D}_D][\mathbf{B}_p]d\mathbf{x}\,d\mathbf{y} \quad \text{and} \quad [\mathbf{F}^e] = \int_0^{\mathbf{b}_e}\int_0^{\mathbf{a}_e}[\mathbf{N}_t]^T\{\mathbf{f}\}d\mathbf{x}\,d\mathbf{y}
\end{aligned}$$

wherein $\mathbf{a}_e$ and $\mathbf{b}_e$ are the length and width of the element in consideration and the various rigidity matrices are given by

$$\begin{aligned}
&[\mathbf{D}_{tb}] = [\overline{\mathbf{C}}_b^0]\int_{-\mathbf{h}/2}^{\mathbf{h}/2} e^{\lambda(\mathbf{z}+\mathbf{h}/2)}d\mathbf{z} + [\overline{\mathbf{C}}_b^2]\mathbf{h}_p, \quad [\mathbf{D}_{ts}] = [\overline{\mathbf{C}}_s^0]\int_{-\mathbf{h}/2}^{\mathbf{h}/2} e^{\lambda(\mathbf{z}+\mathbf{h}/2)}d\mathbf{z} + [\overline{\mathbf{C}}_s^2]\mathbf{h}_p, \\
&[\mathbf{D}_{trb}] = [\overline{\mathbf{C}}_b^0]\int_{-\mathbf{h}/2}^{\mathbf{h}/2} \mathbf{z}e^{\lambda(\mathbf{z}+\mathbf{h}/2)}d\mathbf{z} + \tfrac{1}{2}(-1)^k[\overline{\mathbf{C}}_b^2]\mathbf{h}_p(\mathbf{h}+\mathbf{h}_p), \quad [\mathbf{D}_{trs}] = [\mathbf{D}_{ts}], \\
&[\mathbf{D}_{rrb}] = [\overline{\mathbf{C}}_b^0]\int_{-\mathbf{h}/2}^{\mathbf{h}/2} \mathbf{z}^2e^{\lambda(\mathbf{z}+\mathbf{h}/2)}d\mathbf{z} + \tfrac{1}{3}[\overline{\mathbf{C}}_b^2]\{(\mathbf{h}/2+\mathbf{h}_p)^3 - \mathbf{h}^3/8\}, \quad [\mathbf{D}_{rrs}] = [\mathbf{D}_{ts}] \\
&[\mathbf{D}_{tp}] = \int_{(-1)^k\mathbf{h}/2}^{(-1)^k(\mathbf{h}/2+\mathbf{h}_p)}(-1)^k[\bar{\mathbf{e}}_b][\mathbf{Z}_p]d\mathbf{z}, \quad [\mathbf{D}_{rp}] = \int_{(-1)^k\mathbf{h}/2}^{(-1)^k(\mathbf{h}/2+\mathbf{h}_p)}(-1)^k\mathbf{z}[\bar{\mathbf{e}}_b][\mathbf{Z}_p]d\mathbf{z} \quad \text{and} \\
&[\mathbf{D}_D] = \int_{\mathbf{h}/2}^{\mathbf{h}/2+\mathbf{h}_p}[\mathbf{Z}_p]^T[\bar{\boldsymbol{\epsilon}}][\mathbf{Z}_p]d\mathbf{z}
\end{aligned}$$

At this point, it may be noted that since the elemental bending and shear stiffness matrices are formulated separately, the selective integration scheme can be employed in a straight forward manner to compute these matrices. Applying the principle of minimum total potential energy i.e. $\delta\mathbf{T}_P^e = 0$, the following governing equations of equilibrium of an element are obtained:

$$[\mathbf{K}_t^e]\{\mathbf{d}_t^e\} + [\mathbf{K}_{tr}^e]\{\mathbf{d}_r^e\} = [\mathbf{F}_{tp}^e]\{\boldsymbol{\phi}_0^e\} + \{\mathbf{F}^e\} \tag{27}$$

$$[\mathbf{K}_{rt}^e]\{\mathbf{d}_t^e\} + [\mathbf{K}_{rr}^e]\{\mathbf{d}_r^e\} = [\mathbf{F}_{rp}^e]\{\boldsymbol{\phi}_0^e\} \tag{28}$$

It should be noted here that for activating the PFRC layer, electric potential (voltage) will be specified at the top surface of the PFRC layer. Thus, $\boldsymbol{\delta}\{\boldsymbol{\phi}_0^e\}$ will be zero leading to the derivation of the above governing equations for the element.

Upon assembling the elemental governing equations into global space, the global equations of equilibrium are obtained as follows:

$$[\mathbf{K}_t]\{\mathbf{X}_t\} + [\mathbf{K}_{tr}]\{\mathbf{X}_r\} = [\mathbf{F}_{tp}]\{\boldsymbol{\Phi}\} + \{\mathbf{F}\} \tag{29}$$

$$[\mathbf{K}_{rt}]\{\mathbf{X}_t\} + [\mathbf{K}_{rr}]\{\mathbf{X}_r\} = [\mathbf{F}_{rp}]\{\boldsymbol{\Phi}\} \tag{30}$$

in which, $[\mathbf{K}_t]$, $[\mathbf{K}_{tr}]$ and $[\mathbf{K}_{rr}]$ are the global stiffness matrices; $[\mathbf{F}_{tp}]$ and $[\mathbf{F}_{rp}]$ are the global electro-elastic coupling matrices; $\{\mathbf{X}_t\}$ and $\{\mathbf{X}_r\}$ are the global nodal generalized displacement vectors; $\{\mathbf{F}\}$ is the global nodal mechanical force vector and $\{\boldsymbol{\Phi}\}$ is the global nodal electric potential vector. After imposing the displacement boundary conditions, the global rotational degrees of freedom can be condensed to obtain the global equilibrium equation in terms of the global nodal translational degrees of freedom only as follows:

$$[\mathbf{K}]\{\mathbf{X}_t\} = [\mathbf{F}_{tp}^*]\{\boldsymbol{\Phi}\} + \{\mathbf{F}\} \tag{31}$$

in which, $[\mathbf{K}] = [\mathbf{K}_t] - [\mathbf{K}_{tr}][\mathbf{K}_{rr}]^{-1}[\mathbf{K}_{rt}]$ and $[\mathbf{F}_{tp}{}^*] = [\mathbf{F}_{tp}] - [\mathbf{K}_{tr}][\mathbf{K}_{rr}]^{-1}[\mathbf{F}_{rp}]$. Eq. (31) represents the electro-elastic finite element model of the functionally graded plate integrated with a layer of the PFRC material considered in this study.

3. Numerical results

In this section, the numerical results are evaluated using the finite element model derived in the previous section. The thickness of the substrate FG plate is considered as 3 mm and that of the PFRC layer is taken as 250 μm. The following elastic properties of the material of the substrate FG plate located at the bottom surface of the plate are considered for the numerical results:

$$\mathbf{E}_0 = 200\ GPa \quad \text{and} \quad \boldsymbol{v} = 0.3$$

in which v is the Poison's ratio of the **FGM**. The piezoelectric fiber and the matrix of the PFRC layer are made of PZT5H and **epoxy**, respectively. Considering 40% fiber volume fraction, the following elastic and piezoelectric co-efficients of the PFRC layer are obtained by using the micro-mechanics model derived earlier by one of the author (Mallik and Ray, 2003) of this paper and are used for computing the numerical results.

$$\mathbf{C}_{11} = 32.6\ \text{GPa}, \quad \mathbf{C}_{12} = 4.3\ \text{GPa}, \quad \mathbf{C}_{22} = 7.2\ \text{GPa}, \quad \mathbf{C}_{44} = 1.05\text{GPa}, \quad \mathbf{C}_{55} = \mathbf{C}_{66} = 1.29\ \text{GPa},$$

$$\mathbf{e}_{31} = -6.76\ \text{C/m}^2, \quad \boldsymbol{\epsilon}_{11} = \boldsymbol{\epsilon}_{22} = 0.037\mathbf{e} - 9\ \text{C}/Vm, \quad \boldsymbol{\epsilon}_{33} = 10.64\mathbf{e} - 9\ \text{C/Vm}$$

It has been found from the micro-mechanical analysis (Mallik and Ray, 2003), that the values of other piezoelectric coefficients $\mathbf{e}_{32}$, $\mathbf{e}_{33}$, $\mathbf{e}_{15}$ and $\mathbf{e}_{24}$ with respect to the material coordinate system are negligibly smaller than that of $\mathbf{e}_{31}$ and hence are not considered to evaluate the numerical results.

The results are evaluated with and without applying the electrical potential distribution on the actuator surface for different values of length to thickness ratio **s** (=**a**/**h**) of the FG plate. The following non-dimensional parameters are used for presenting the numerical results.

$$\bar{\mathbf{u}} = \frac{\mathbf{E}_0\mathbf{u}}{|\mathbf{f}_0|\mathbf{s}^3\mathbf{h}}, \quad \bar{\mathbf{w}} = \frac{100\mathbf{E}_0\mathbf{w}_0}{|\mathbf{f}_0|\mathbf{s}^4\mathbf{h}}, \quad \bar{\boldsymbol{\sigma}}_{bfx} = \frac{\boldsymbol{\sigma}_\mathbf{x}}{|\mathbf{f}_0|\mathbf{s}^2}, \quad \bar{\boldsymbol{\sigma}}_y = \frac{\boldsymbol{\sigma}_\mathbf{y}}{|\mathbf{f}_0|\mathbf{s}^2} \quad \text{and} \quad \bar{\boldsymbol{\sigma}}_{\mathrm{xy}} = \frac{\boldsymbol{\sigma}_{\mathrm{xy}}}{|\mathbf{f}_0|\mathbf{s}^2}$$

In which, $\mathbf{f}_0$ is either the amplitude of the applied distributed sinusoidal load (SSL) or the intensity of the applied uniformly distributed load (UDL). The prescribed electric potential distribution on the exposed surface of the PFRC layer is considered either as spatially distributed sinusoidal electric potential or uniformly distributed electric potential with amplitude V (volt). Unless otherwise mentioned, the piezoelectric fiber orientation (ψ) in the PFRC layer is considered as zero degree. The following simply-supported boundary conditions (Ray and Sachade, accepted for publication) are used to evaluate the numerical results:

$$\mathbf{v}_0 = \mathbf{w} = \boldsymbol{\theta}_y = 0 \quad \text{at } \mathbf{x} = 0, \mathbf{a} \quad \text{and} \quad \mathbf{u}_0 = \mathbf{w} = \boldsymbol{\theta}_\mathbf{X} = 0 \quad \text{at } \mathbf{y} = 0, \mathbf{b}$$

Considering the amplitude of distributed sinusoidal mechanical load as $\mathbf{f}_0 = -40\ \mathrm{N/m^2}$, the mechanical displacements ($\mathbf{u}$ and $\mathbf{w}$) and in-plane stresses ($\boldsymbol{\sigma}_\mathbf{x}$, $\boldsymbol{\sigma}_\mathrm{y}$ and $\boldsymbol{\sigma}_{\mathrm{xy}}$) in the substrate FG plates are computed with and without applying the spatially distributed sinusoidal electric potential on the surface of the PFRC layer being attached at the top surface of the substrate FG plate and are compared with the exact solutions derived by the authors (Ray and Sachade, accepted for publication). These results are provided in Tables 1 and 2 for $\mathbf{E}_\mathrm{h}/\mathbf{E}_0 = 10$ and 0.1, respectively. Note that $\mathbf{E}_\mathrm{h}$ is the Young's modulus of the material located at the top surface of the FG plate. It may be observed from these tables that the results for both thick

Table 1
Responses of the FG substrate plates ($\mathbf{E}_\mathrm{h}/\mathbf{E}_0 = 10$) with and without the applied sinusoidal voltage to the PFRC layer being integrated with the top surface of the plate

Method	$\mathbf{s} = 10$			$\mathbf{s} = 20$			$\mathbf{s} = 100$		
	$V = 0$	$V = 100$	$V = -100$	$V = 0$	$V = 100$	$V = -100$	$V = 0$	$V = 100$	$V = -100$
Present FEM $\mathbf{u}^*$	−0.0195	0.0459	−0.0849	−0.0195	−0.0297	−0.0093	−0.0195	−0.0202	−0.0187
	0.0093	−5.9402	5.9588	0.0093	−1.4655	1.4840	0.0093	−0.0496	0.0681
Exact solution $\mathbf{u}^*$	−0.0194	−0.0307	−0.0081	−0.0195	−0.0337	−0.0053	−0.0195	−0.0202	−0.0188
Ray and Sachade (accepted for publication)	0.0093	−5.9373	5.9558	0.0093	−1.4670	1.4855	0.0093	−0.0497	0.0682
Present FEM $\mathbf{w}^*$	−0.9485	183.9178	−185.8148	−0.9233	45.2938	−47.1403	−0.9145	0.9328	−2.7619
Exact solution $\mathbf{w}^*$	−0.9553	186.8222	−188.7329	−0.9252	45.5393	−47.3897	−0.9155	0.9368	−2.7678
Ray and Sachade (accepted for publication)									
Present EM $\boldsymbol{\sigma}^*_\mathbf{x}$	0.0893	−6.1985	6.3772	0.0893	−1.4170	1.5957	0.0893	0.0299	0.1486
	−0.4250	208.1946	−209.0447	−0.4250	51.4183	−52.2684	−0.4247	1.6447	−2.4941
Exact solution σ^*_x	0.0871	−5.8052	5.9794	0.0873	−1.3742	1.5489	0.0874	0.0291	0.1457
Ray and Sachade (accepted for publication)	−0.4201	203.984	−204.8249	−0.4171	50.3911	−51.2253	−0.4161	1.6124	−2.4446
Present FEM $\boldsymbol{\sigma}^*_y$	0.0893	−20.1638	20.3424	0.0893	−5.0400	5.2185	0.0892	−0.1167	0.2951
	−0.4260	58.2432	−59.0951	−0.4259	14.5560	−15.4079	−0.4256	0.1772	−1.0283
Exact solution $\boldsymbol{\sigma}^*_y$	0.0870	−19.6720	19.8460	0.0872	−4.9333	5.1078	0.0873	−0.1145	0.2892
Ray and Sachade (accepted for publication)	−0.4213	57.9752	−58.8178	−0.4180	14.3338	−15.1698	−0.4170	0.1751	−1.0090
Present FEM $\boldsymbol{\sigma}_{\mathrm{xy}}{}^*$	−0.0481	7.1027	−7.1989	−0.0481	1.7394	−1.8356	−0.0480	0.0233	−0.1194
	0.2290	−71.7882	72.2462	0.2290	−17.7746	18.2326	0.2289	−0.4907	0.9486
Exact solution $\boldsymbol{\sigma}_{\mathrm{xy}}{}^*$	−0.0469	6.8593	−6.9530	−0.0470	1.6982	−1.7922	−0.0470	0.0230	−0.1171
Ray and Sachade (accepted for publication)	0.2242	−70.4771	70.9256	0.2243	−17.4232	17.8717	0.2243	−0.4813	0.9298

Where $\mathbf{u}^* = \bar{\mathbf{u}}_{(0,b/2,\mp h/2)}$, $\mathbf{w}^* = \bar{\mathbf{w}}_{(a/2,b/2,0)}$, $(\boldsymbol{\sigma}^*_\mathbf{X}, \boldsymbol{\sigma}^*_\mathbf{y}) = (\bar{\boldsymbol{\sigma}}_\mathbf{X}, \bar{\boldsymbol{\sigma}}_\mathbf{y})_{(a/2,b/2,\mp h/2)}$ and $\boldsymbol{\sigma}^*_{\mathbf{xy}} = \bar{\boldsymbol{\sigma}}_{\mathrm{xy}(0,0,\mp h/2)}$.

Table 2
Responses of the FG substrate plates ($\mathbf{E}_h/\mathbf{E}_0 = 0.1$) with and without the applied sinusoidal voltage to the PFRC layer being integrated with the top surface of the plate

	$\mathbf{s} = 10$			$\mathbf{s} = 20$			$\mathbf{s} = 100$		
	$V = 0$	$V = 100$	$V = -100$	$V = 0$	$V = 100$	$V = -100$	$V = 0$	$V = 100$	$V = -100$
Present FEM $\mathbf{u}^*$	−0.0901	−3.0418	2.8616	−0.0902	−1.0641	0.8838	−0.0901	−0.1322	−0.0480
	0.1714	−107.7880	108.1308	0.1716	−26.3653	26.7085	0.1715	−0.8840	1.2270
Exact solution $\mathbf{u}^*$	−0.0914	−3.1845	3.0017	−0.0912	−0.9839	0.8015	−0.0912	−0.1285	−0.0539
Ray and Sachade (accepted for publication)	0.1686	−114.0117	114.3489	0.1735	−27.0971	27.4441	0.175	−0.8991	1.2493
Present FEM $\mathbf{w}^*$	−8.6673	3212.9	−3230.3	−8.4154	797.9455	−814.7764	−8.3292	23.9160	−40.5745
Exact solution $\mathbf{w}^*$	−8.7397	3253.3	−3270.8	−8.5437	813.7105	−830.7979	−8.4806	24.4974	−41.4587
Ray and Sachade (accepted for publication)									
Present EM $\boldsymbol{\sigma}^*_{\mathbf{x}}$	0.4066	−42.1225	42.9357	0.4068	−9.6579	10.4715	0.4066	0.0119	0.8013
	−0.0793	43.0275	−43.1862	−0.0794	10.5905	−10.7493	−0.0793	0.3460	−0.5046
Exact solution $\boldsymbol{\sigma}^*_{\mathbf{x}}$	0.4042	−41.0915	41.8999	0.4031	−9.8557	10.6619	0.4027	−0.0061	0.8115
Ray and Sachade (accepted for publication)	−0.0807	44.3075	−44.4689	−0.0796	10.6491	−10.8083	−0.0793	0.3451	−0.5036
Present FEM $\boldsymbol{\sigma}^*_{\mathbf{y}}$	0.3916	−172.902	173.6851	0.3913	−43.5671	44.3496	0.3909	−1.3748	2.1565
	−0.0810	28.0609	−28.2229	−0.0810	7.0834	−7.2453	−0.0809	0.2072	−0.3689
Exact solution $\boldsymbol{\sigma}^*_{\mathbf{y}}$	0.3900	−170.3199	171.0999	0.3883	−43.1562	43.9327	0.3877	−1.3654	2.1408
Ray and Sachade (accepted for publication)	−0.0825	28.1032	−28.2681	−0.0812	7.1105	−7.2729	−0.0808	0.2088	−0.3704
Present FEM $\boldsymbol{\sigma}^*_{\mathbf{xy}}$	−0.2148	57.9332	−58.3627	−0.2148	14.3377	−14.7673	−0.2147	0.3667	−0.7962
	0.0431	−19.1536	19.2399	0.0431	−4.7614	4.8477	0.0431	−0.1489	0.2352
Exact solution $\boldsymbol{\sigma}^*_{\mathbf{xy}}$	−0.2138	56.9184	−57.3461	−0.2131	14.2724	−4.6986	−0.2128	0.3692	−0.7948
Ray and Sachade (accepted for publication)	0.0416	−19.4500	19.5333	0.0427	−4.7790	4.8645	0.0431	−0.1491	0.2353

Where $\mathbf{u}^* = \bar{\mathbf{u}}_{(0,b/2,\,\mp h/2)}, \mathbf{w}^* = \bar{\mathbf{w}}_{(a/2,b/2,0)}, (\boldsymbol{\sigma}^*_{\mathbf{x}}, \boldsymbol{\sigma}^*_{\mathbf{y}}) = (\bar{\boldsymbol{\sigma}}_{\mathbf{x}}, \bar{\boldsymbol{\sigma}}_{\mathbf{y}})_{(a/2,b/2,\mp h/2)}$ and $\boldsymbol{\sigma}^*_{\mathbf{xy}} = \bar{\boldsymbol{\sigma}}_{xy(0,0,\mp h/2)}$.

and thin substrate FG plates obtained by the present FEM match excellently with those obtained by the exact solutions. A further comparison with the exact solutions is also illustrated in Tables 3 and 4 which manifest the performance of the PFRC layer when it is attached at the bottom surface of the FG plates, for $\mathbf{E}_h/\mathbf{E}_0 = 10$ and 0.1, respectively. It may again be observed from these tables that the finite element model derived here accurately predicts the response of the FG plates under the actions of the mechanical and electric loads when the PFRC layer is bonded to the bottom of the FG plates. Thus the present finite element model can be reliably used for the analysis of both thick and thin functionally graded smart plates.

Next, considering that the PFRC layer being attached at the top surface of the FG plate, the responses of the substrate FG plates are computed using this finite element model when the plates are subjected to a uniformly distributed mechanical load ($\mathbf{f}_0 = -40\ \mathrm{N/m^2}$) and the PFRC layer is activated with a uniformly distributed electric potential on its exposed surface. Tables 5 and 6 contain these responses for both thick and thin FG plates with $\mathbf{E}_h/\mathbf{E}_0 = 10$ and 0.1, respectively.

An important aspect of developing this finite element model is to investigate the effect of variation of fiber orientation ($\boldsymbol{\psi}$) in the PFRC layer on its capability of actuating the FG substrate plates. Fig. 2 illustrates this effect of variation of the piezoelectric fiber orientation ($\boldsymbol{\psi}$) in the PFRC layer on the center deflection of the FG substrate plate for which $\mathbf{E}_h/\mathbf{E}_0 = 10$. For this, a prescribed uniformly distributed electric potential is considered on the exposed surface of the PFRC layer such that the resultant deflection under the combined action of mechanical and electrical load becomes opposite to that caused by the uniformly

Table 3
Responses of the FG substrate plates ($\mathbf{E_h/E_0} = 10$) with and without the applied sinusoidal voltage to the PFRC layer being integrated with the bottom surface of the plate

Method	$\mathbf{s} = 10$			$\mathbf{s} = 20$			$\mathbf{s} = 100$		
	$V = 0$	$V = 100$	$V = -100$	$V = 0$	$V = 100$	$V = -100$	$V = 0$	$V = 100$	$V = -100$
Present FEM $\mathbf{u}^*$	−0.0193	11.9237	−11.9622	−0.0193	2.9147	−2.9532	−0.0192	0.0974	−0.1359
	0.0093	0.1967	−0.1781	0.0093	0.0811	−0.0625	0.0093	0.0125	0.0061
Exact solution $\mathbf{u}^*$	−0.0192	12.4664	−12.5049	−0.0193	2.9557	−2.9942	−0.0193	0.0978	−0.1364
Ray and Sachade (accepted for publication)	0.0093	0.2578	−0.2391	0.0093	0.0835	−0.0649	0.0093	0.0124	0.0062
Present FEM $\mathbf{w}^*$	−0.9416	360.3108	−362.1940	−0.9164	89.4064	−91.2392	−0.9076	2.7028	−4.5180
Exact solution $\mathbf{w}^*$	−0.9428	359.0874	−360.9938	−0.9205	89.5468	−91.3877	−0.9100	2.7147	−4.5346
Ray and Sachade (accepted for publication)									
Present EM $\boldsymbol{\sigma}^*_{\mathbf{x}}$	0.0883	−47.8463	48.0230	0.0883	−11.7681	11.9448	0.0883	−0.3842	0.5608
	−0.4250	50.8126	−51.6626	−0.4250	11.7704	−12.6204	−0.4246	0.0546	−0.9039
Exact solution $\boldsymbol{\sigma}^*_{\mathbf{x}}$	0.0865	−48.6233	48.7963	0.0866	−11.6559	11.8291	0.0866	−0.3775	0.5507
Ray and Sachade (accepted for publication)	−0.4228	47.6247	−48.4703	−0.4179	11.4491	−12.2848	−0.4163	0.0564	−0.8890
Present FEM $\boldsymbol{\sigma}^*_{\mathbf{y}}$	0.0885	−31.8707	32.0478	0.0885	−8.0314	8.2085	0.0885	−0.2378	0.4147
	−0.4233	190.3620	−191.2086	−0.4232	47.8967	−48.7431	−0.4229	1.5168	−2.3626
Exact solution $\boldsymbol{\sigma}^*_{\mathbf{y}}$	0.0867	−31.3030	31.4763	0.0868	−7.8872	8.0607	0.0868	−0.2338	0.4074
Ray and Sachade (accepted for publication)	−0.4212	185.7531	−186.5955	−0.4162	46.9151	−47.7476	−0.4146	1.4889	−2.3181
Present FEM $\boldsymbol{\sigma}^*_{\mathbf{xy}}$	−0.0476	21.4743	−21.5695	−0.0476	5.3330	−5.4282	−0.0476	0.1674	−0.2626
	0.2282	64.9662	65.4226	0.2282	−16.0699	16.5264	0.2282	−0.4228	0.8791
Exact solution $\boldsymbol{\sigma}^*_{\mathbf{xy}}$	−0.0466	21.4662	−21.5594	−0.0467	5.2583	−5.3516	−0.0467	0.1646	−0.2579
Ray and Sachade (accepted for publication)	0.2249	−62.8348	63.2847	0.2240	−15.7140	16.1620	0.2237	−0.4161	0.8634

Where $\mathbf{u}^* = \bar{\mathbf{u}}_{(0,b/2,\mp h/2)}$, $\mathbf{w}^* = \bar{\mathbf{w}}_{(a/2,b/2,0)}$, $(\boldsymbol{\sigma}^*_{\mathbf{x}}, \boldsymbol{\sigma}^*_{\mathbf{y}}) = (\bar{\boldsymbol{\sigma}}_{\mathbf{x}}, \bar{\boldsymbol{\sigma}}_{\mathbf{y}})_{(a/2,b/2,\mp h/2)}$ and $\boldsymbol{\sigma}^*_{\mathbf{xy}} = \bar{\boldsymbol{\sigma}}_{xy(0,0,\mp h/2)}$.

distributed mechanical load alone acting vertically downward only. Thus, the more is the resultant deflection under the combined action of mechanical and electrical load the more will be the control authority of the activated PFRC layer. It may be observed from Fig. 2 that for the FG plate with $\mathbf{E_h/E_0} = 10$ the actuating capability of the PFRC layer is almost independent of the variation of the piezoelectric fiber angle. But the actuating capability of the PFRC layer which is attached at the bottom surface of this FG plate is greater than that of the PFRC layer which is bonded to the top surface of this FG plate. Fig. 3 illustrates the effect of fiber orientation in the PFRC layer on the control of center deflection of the FG plate with $\mathbf{E_h/E_0} = 0.1$. From this figure it may be observed that the performance of the PFRC layer when attached at the bottom of the FG plate is negligibly affected by the variation of the piezoelectric fiber angle ($\boldsymbol{\psi}$) in the PFRC layer while the performance of the activated PFRC layer when attached at the top surface of this FG plate is slightly sensitive to the variation of the piezoelectric fiber angle ($\boldsymbol{\psi}$) in the PFRC layer and becomes maximum if the value of $\boldsymbol{\psi}$ is 0° or 90°. Also, in case of the FG plate with $\mathbf{E_h/E_0} = 0.1$, as opposed to the FG plate with $\mathbf{E_h/E_0} = 10$, the actuating capability of the PFRC layer being attached to the top surface of the plate becomes greater than that of the PFRC layer being attached at the bottom of the plate.

Finally, the variation of normal stress ($\boldsymbol{\sigma}_{\mathbf{x}}$) across the thickness of the FG substrate plates due to the combined action of the spatially uniform electric potential on the surface of the PFRC layer and the applied mechanical load ($\mathbf{f}_0 = -40\ \mathrm{N/m^2}$) has been illustrated in Figs. 4 and 5 for a thin ($\mathbf{s} = 100$) FG plate ($\mathbf{E_h/E_0} = 10$) with the PFRC actuator layer being attached to the top and bottom surfaces of the plate,

Table 4
Responses of the FG substrate plates ($\mathbf{E_h/E_0} = 0.1$) with and without the applied sinusoidal voltage to the PFRC layer being integrated with the bottom surface of the plate

	$\mathbf{s} = 10$			$\mathbf{s} = 20$			$\mathbf{s} = 100$		
	$V = 0$	$V = 100$	$V = -100$	$V = 0$	$V = 100$	$V = -100$	$V = 0$	$V = 100$	$V = -100$
Present FEM **u***	−0.0877	56.9037	−57.0792	−0.0878	14.0431	−14.2186	−0.0877	0.4760	−0.6514
	0.1931	−0.0201	0.4063	0.1932	0.3963	−0.0100	0.1930	0.2046	0.1815
Exact solution **u***	−0.0890	57.1020	−57.2801	−0.0886	14.1124	−14.2896	−0.0885	0.4783	−0.6552
Ray and Sachade (accepted for publication)	0.1890	0.5288	−0.1507	0.1925	0.3882	−0.0032	0.1936	0.2029	0.1844
Present FEM **w***	−9.2748	1748.2	−1766.7	−9.0233	430.4678	−448.5145	−8.9364	8.6323	−26.5051
Exact solution **w***	−9.2761	1789.0	−1807.5	−9.0549	436.0142	−454.1240	−8.9838	8.7587	−26.7281
Ray and Sachade (accepted for publication)									
Present EM $\boldsymbol{\sigma}^*_{\mathbf{X}}$	0.4060	−198.9894	199.8015	0.4061	−49.1587	49.9708	0.4058	−1.5729	2.3844
	−0.0882	5.7883	−5.9647	−0.0882	1.3181	−1.4945	−0.0881	−0.0328	−0.1435
Exact solution $\boldsymbol{\sigma}^*_{\mathbf{X}}$	0.4032	−195.9356	196.7419	0.4011	−48.4127	49.2150	0.4005	−1.5486	2.3495
Ray and Sachade (accepted for publication)	−0.0888	5.4977	−5.6753	−0.0871	1.2984	−1.4726	−0.0866	−0.0313	−0.1419
Present FEM $\boldsymbol{\sigma}^*_{\mathbf{y}}$	0.4148	−54.2976	55.1272	0.4147	−13.5690	14.3984	0.4143	−0.1484	0.9771
	−0.0874	19.2664	−19.4412	−0.0874	4.8161	−4.9909	−0.0873	0.1096	−0.2842
Exact solution $\boldsymbol{\sigma}^*_{\mathbf{y}}$	0.4115	−54.9286	55.7515	0.4093	−13.5769	14.3954	0.4085	−0.1529	0.9700
Ray and Sachade (accepted for publication)	−0.0880	18.8895	−19.0655	−0.0863	4.7369	−4.9096	−0.0858	0.1082	−0.2798
Present FEM $\boldsymbol{\sigma}^*_{\mathbf{xy}}$	−0.2208	68.2317	−68.6734	−0.2209	16.8966	−17.3383	−0.2208	0.4635	−0.9051
	0.0472	−6.7491	6.8436	0.0472	−1.6521	1.7466	0.0472	−0.0207	0.1151
Exact solution $\boldsymbol{\sigma}^*_{\mathbf{xy}}$	−0.2193	67.4898	−67.9285	−0.2182	16.6863	−17.1227	−0.2178	0.4581	−0.8937
Ray and Sachade (accepted for publication)	0.0453	−6.5681	6.6587	0.0461	−1.6255	1.7177	0.0464	−0.0207	0.1135

Where $\mathbf{u}^* = \bar{\mathbf{u}}_{(0,b/2,\mp h/2)}$, $\mathbf{w}^* = \bar{\mathbf{w}}_{(a/2,b/2,0)}$, $(\boldsymbol{\sigma}^*_{\mathbf{X}}, \boldsymbol{\sigma}^*_{\mathbf{y}}) = (\bar{\boldsymbol{\sigma}}_{\mathbf{X}}, \bar{\boldsymbol{\sigma}}_{\mathbf{y}})_{(a/2,b/2,\mp h/2)}$ and $\boldsymbol{\sigma}^*_{\mathbf{xy}} = \bar{\boldsymbol{\sigma}}_{\mathbf{xy}(0,0,\mp h/2)}$.

Table 5
Responses of the FG substrate plates ($\mathbf{E_h/E_0} = 10$) subjected to uniformly distributed mechanical load when the PFRC layer being attached at the top of the plate is activated by uniformly distributed voltage

	$\mathbf{s} = 10$			$\mathbf{s} = 20$			$\mathbf{s} = 100$		
	$V = 0$	$V = 100$	$V = -100$	$V = 0$	$V = 100$	$V = -100$	$V = 0$	$V = 100$	$V = -100$
u*	−0.0326	3.6820	−3.7471	−0.0326	0.8600	−0.9252	−0.0326	0.0050	−0.0702
	0.0155	−12.5076	12.5385	0.0155	−3.0982	3.1291	0.0155	−0.1100	0.1409
w*	−1.4965	267.5554	−270.5485	−1.4597	65.8056	−68.7251	−1.4468	1.2361	−4.1297
$\boldsymbol{\sigma}^*_{\mathbf{X}}$	0.1285	0.2811	−0.0240	0.1285	0.2053	0.0517	0.1283	0.1373	0.1194
	−0.6115	200.6055	−201.8286	−0.6115	49.5096	−50.7326	−0.6106	1.3661	−2.5874
$\boldsymbol{\sigma}^*_{\mathbf{y}}$	0.1284	−25.5282	25.7850	0.1284	−6.3218	6.5785	0.1282	−0.1295	0.3859
	−0.6127	55.2329	−56.4584	−0.6127	13.5196	−14.7450	−0.6118	−0.0480	−1.1757
$\boldsymbol{\sigma}^*_{\mathbf{xy}}$	−0.0876	28.0091	−28.1844	−0.0875	6.4533	−6.6283	−0.0862	0.1161	−0.2886
	0.4176	−292.1229	292.9581	0.4170	−70.4208	71.2549	0.4110	−2.1401	2.9620

Where $\mathbf{u}^* = \bar{\mathbf{u}}_{(0,b/2,\mp h/2)}$, $\mathbf{w}^* = \bar{\mathbf{w}}_{(a/2,b/2,0)}$, $(\boldsymbol{\sigma}^*_{\mathbf{X}}, \boldsymbol{\sigma}^*_{\mathbf{y}}) = (\bar{\boldsymbol{\sigma}}_{\mathbf{X}}, \bar{\boldsymbol{\sigma}}_{\mathbf{y}})_{(a/2,b/2,\mp h/2)}$ and $\boldsymbol{\sigma}^*_{\mathbf{xy}} = \bar{\boldsymbol{\sigma}}_{xy(0,0,\mp h/2)}$.

Table 6
Responses of the FG substrate plates ($\mathbf{E_h/E_0} = 0.1$) subjected to uniformly distributed mechanical load when the PFRC layer being attached at the top of the plate is activated by uniformly distributed voltage

	$\mathbf{s} = 10$			$\mathbf{s} = 20$			$\mathbf{s} = 100$		
	$V = 0$	$V = 100$	$V = -100$	$V = 0$	$V = 100$	$V = -100$	$V = 0$	$V = 100$	$V = -100$
$\mathbf{u}^*$	−0.1499	22.3291	−22.6289	−0.1501	5.1648	−5.4650	−0.1502	0.0791	−0.3795
	0.2849	−248.0636	248.6334	0.2853	−61.2189	61.7894	0.2856	−2.2066	2.7778
$\mathbf{w}^*$	−13.6786	4715.2	−4742.5	−13.3114	1170.3	−1196.9	−13.1840	34.0498	−60.4177
$\boldsymbol{\sigma}^*_{\mathbf{x}}$	0.5885	6.6564	−5.4795	0.5888	2.5040	−1.3264	0.5880	0.7116	0.4643
	−0.1149	38.6320	−38.8617	−0.1149	9.5003	−9.7302	−0.1148	0.2609	−0.4905
$\boldsymbol{\sigma}^*_{\mathbf{y}}$	0.5619	−222.8476	223.9714	0.5614	−55.7100	56.8328	0.5606	−1.6919	2.8130
	−0.1166	33.0344	−33.2676	−0.1165	8.2523	−8.4853	−0.1163	0.2188	−0.4514
$\boldsymbol{\sigma}^*_{\mathbf{xy}}$	−0.3904	216.5978	−217.3786	−0.3897	49.4226	−50.2021	−0.3843	1.1098	−1.8783
	0.0786	−75.7193	75.8766	0.0785	−18.0189	18.1759	0.0774	−0.5464	0.7011

Where $\mathbf{u}^* = \bar{\mathbf{u}}_{(0,b/2,\mp h/2)}$, $w^* = \bar{\mathbf{w}}_{(a/2,b/2,0)}$, $(\boldsymbol{\sigma}^*_{\mathbf{X}}, \boldsymbol{\sigma}^*_{\mathbf{y}}) = (\bar{\boldsymbol{\sigma}}_{\mathbf{X}}, \bar{\boldsymbol{\sigma}}_{\mathbf{y}})_{(a/2,b/2,\mp h/2)}$ and $\boldsymbol{\sigma}^*_{\mathbf{xy}} = \bar{\boldsymbol{\sigma}}_{xy(0,0,\mp h/2)}$.

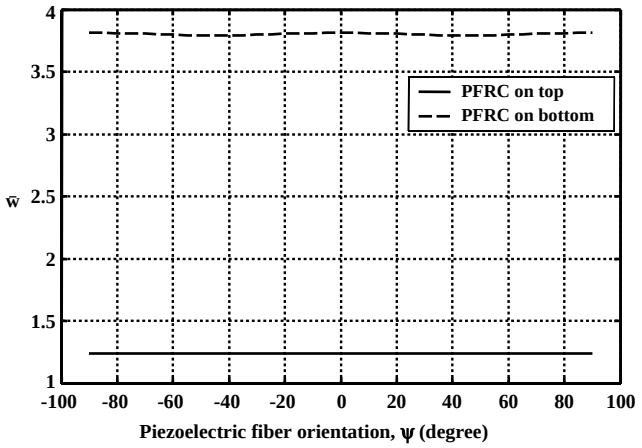

Fig. 2. Variation of the center deflection $\bar{\mathbf{w}}_{(\mathbf{a}/2,\mathbf{b}/2,0)}$ of an FG plate ($\mathbf{E_h/E_0} = 10$, $\mathbf{s} = 100$) with the piezoelectric fiber angle $\boldsymbol{\psi}$ in the PFRC layer, ($V = 100$ V).

respectively. It may be observed from these figures that the distribution of normal stress $\boldsymbol{\sigma}_{\mathbf{x}}$ across the thickness of the FG plate is nonlinear and is highly affected by the activated PFRC layer. In case of the FG plate with $\mathbf{E_h/E_0} = 10$, the Young's modulus of the materials located at the top surface of this plate is maximum. As a result, the activated PFRC layer causes maximum stress concentration at the top surface of this plate. If the PFRC layer is attached at the top or bottom surface of this FG plate then the maximum stress concentration occurs for the value of the piezoelectric fiber angle in the PFRC layer as 0° or 90°, respectively. Figs. 6 and 7 illustrate the effect of fiber orientation in the PFRC layer on the distribution of normal stress $\boldsymbol{\sigma}_{\mathbf{x}}$ across the thickness of the FG plate with $\mathbf{E_h/E_0} = 0.1$ under the action of activated PFRC layer against the uniformly distributed mechanical load ($\mathbf{f}_0 = -40\ \mathrm{N/m^2}$). For this plate, the stress concentration becomes maximum at the bottom surface of the plate as the materials located at the bottom the plate are stiffest. If the fiber angle in the PFRC layer is 90° and the PFRC layer is attached at the top of this FG plate

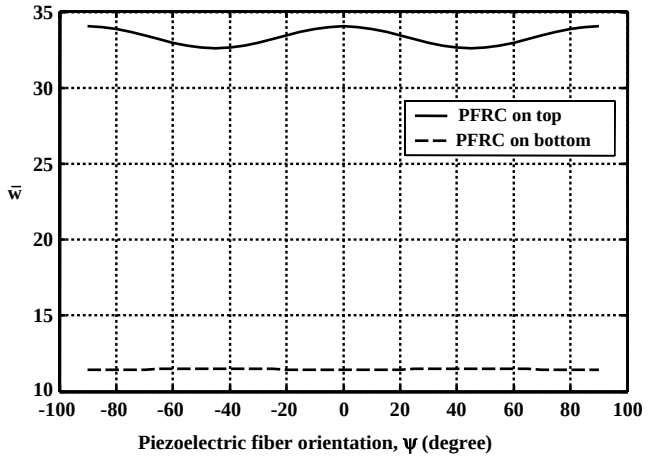

Fig. 3. Variation of the center deflection $\bar{w}_{(a/2,b/2,0)}$ of an FG plate ($E_h/E_0 = 0.1$, $s = 100$) with the piezoelectric fiber angle ψ in the PFRC layer, ($V = 100$ V).

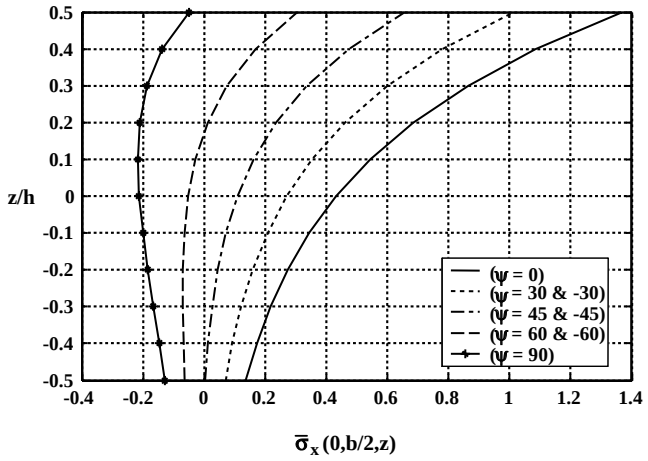

Fig. 4. Distribution of in-plane normal stress $\bar{\sigma}_X$ across the thickness of a thin FG plate ($E_h/E_0 = 10$, $s = 100$) for different fiber orientation ψ in the activated PFRC layer ($V = 100$ V) attached at the top of the plate.

then the stress concentration becomes maximum while for the PFRC layer bonded to the bottom of this FG plate, the maximum stress concentration occurs when the fiber angle in the PFRC layer is 0°. Figs. 4–7 also revealed that that the distribution of normal stress across the thickness of the FG substrate plates due to the action of activated PFRC layer is not sensitive to the sign of the piezoelectric fiber angle in the PFRC layer.

4. Conclusions

In this paper a finite element model for the static analysis of functionally graded plates integrated with a layer of piezoelectric fiber-reinforced composite (PFRC) material has been developed. The layer of the PFRC material acts as the distributed actuator of the plates. The PFRC material considered here is a

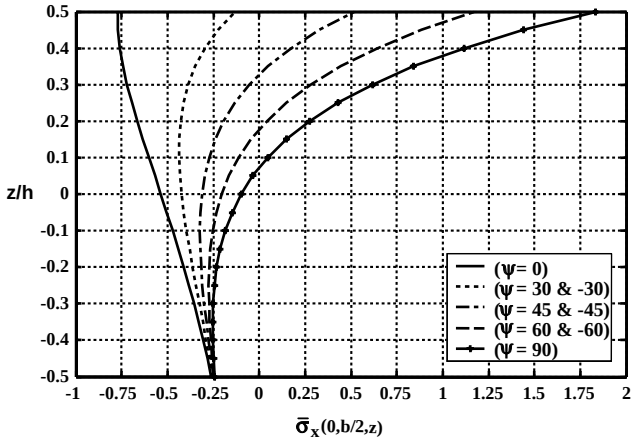

Fig. 5. Distribution of in-plane normal stress $\bar{\sigma}_x$ across the thickness of a thin FG plate ($\mathbf{E}_h/\mathbf{E}_0 = 10$, $\mathbf{s} = 100$) for different fiber orientation ψ in the activated PFRC layer attached at the bottom surface of the plate (V=100 V).

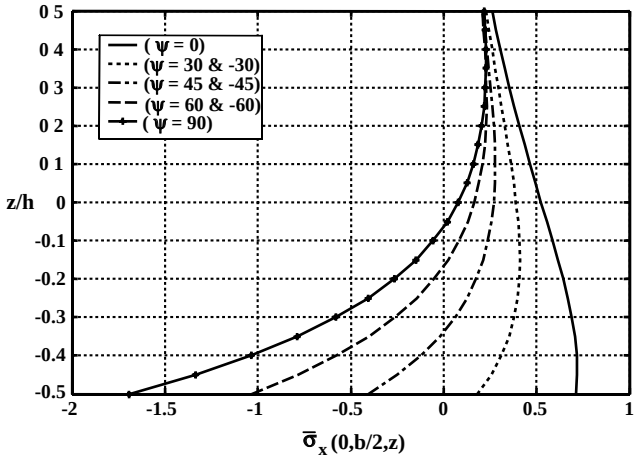

Fig. 6. Distribution of in-plane normal stress $\bar{\sigma}_x$ across the thickness of a thin FG plate ($\mathbf{E}_h/\mathbf{E}_0 = 0.1$, $\mathbf{s} = 100$) for different fiber orientation ψ in the activated PFRC layer ($V = 100$ V) attached at the top of the plate.

new smart material with enhanced effective piezoelectric coefficient as compared to its constituent monolithic counterpart and the piezoelectric fibers are oriented longitudinally in the plane of the FG plates. The Young's modulus of the FG plate has been considered to vary exponentially along the thickness of the plate while the Poisson' ratio of the plate is assumed to be constant over the domain of the plate. The responses of the simply supported smart FG plates under the actions of sinusoidally distributed mechanical load and the PFRC layer activated by the sinusoidally distributed electric potential obtained by this finite element model are compared with the exact solutions for both thick and thin plates. The excellent matching of the results validates the model derived here. The responses of the FG plates under the combined actions of uniformly distributed mechanical load and the uniformly distributed voltage applied to the PFRC layer have also been provided. The investigation of the effect of variation of the piezoelectric fiber orientation on the performance of the activated PFRC layer revealed that in general the performance of the

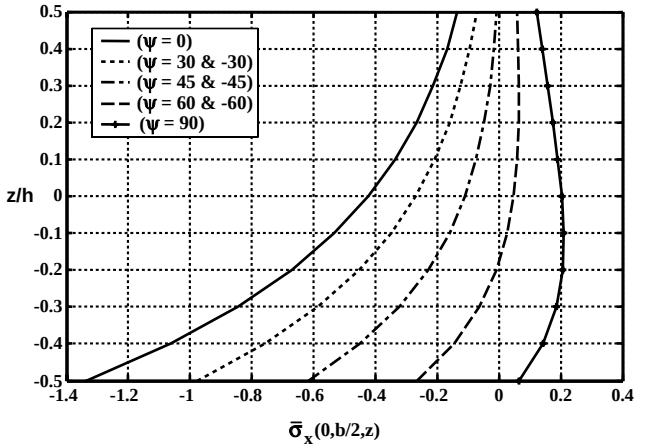

Fig. 7. Distribution of in-plane normal stress $\bar{\sigma}_x$ across the thickness of a thin FG plate ($\mathbf{E}_h/\mathbf{E}_0 = 0.1$, $\mathbf{s} = 100$) for different fiber orientation ψ in the activated PFRC layer attached at the bottom surface of the plate ($V = 100$ V).

PFRC layer becomes maximum if it is integrated with the softest surface of the FG plate. In case of the FG plate for which $\mathbf{E}_h/\mathbf{E}_0 = 0.1$, the actuating capability of the PFRC layer becomes maximum if the values of fiber angle in the PFRC layer is 0° or 90° while for the FG plate with large material gradient ($\mathbf{E}_h/\mathbf{E}_0 = 10$), the actuating capability of the PFRC layer is almost independent of the piezoelectric fiber angle. The distribution of normal stress across the thickness of the FG plates is also affected by the positions of the activated PFRC layer and varies with the variation of the piezoelectric fiber angle. The activated PFRC layer causes maximum stress concentration at that surface (top or bottom) of the FG plates where the materials have the maximum value of the Young's modulus. If the PFRC layer is integrated with the top or bottom surface of the FG plate for which $\mathbf{E}_h/\mathbf{E}_0 = 10$ then the piezoelectric fiber angle in the PFRC layer should be 0° or 90°, respectively to cause maximum induced normal stress in the plate. On the other hand, the piezoelectric fiber angle in the PFRC layer attached at the top and bottom surface of the FG plate with $\mathbf{E}_h/\mathbf{E}_0 = 0.1$ should be 90° and 0°, respectively to induce maximum active normal stress in the plate. It has also been observed that the responses of the smart FG plates are not influenced by the reversal of the sign of the piezoelectric fiber angle in the PFRC layer.

References

Aboudi, J., Pindera, M.J., Arnold, S.M., 1999. Higher-order theory for functionally graded materials. Composites. Part B: Engineering 30 (8), 777–832.

Bailey, T., Hubbard, J.E., 1985. Distributed piezoelectric polymer active vibration control of a cantilever beam. Journal of Guidance, Control and Dynamics 8 (2), 605–611.

Batra, R.C., Vel, S.S., 2001. Exact solution for thermoelastic deformations of functionally graded thick rectangular plates. AIAA Journal 40 (7), 1421–1433.

Baz, A., Poh, S., 1988. Performance of an active control system with piezoelectric actuators. Journal of Sound and Vibration 126, 327–343.

Baz, A., Poh, S., 1996. Optimal vibration control with modal positive position feedback. Optimal Control Applications and Methods 17, 141–149.

Chakraborty, A., Gopalakrishnan, S., 2003. A spectrally formulated finite element for wave propagation analysis in functionally graded beams. International Journal of Solids and Structures 40 (10), 2421–2448.

Chakraborty, A., Gopalakrishnan, S., Reddy, J.N., 2003. A new beam finite element for the analysis of functionally graded materials. International Journal of Mechanical Sciences 45 (3), 519–539.

Chen, B., Tong, L., Gu, Y., Zhang, H., Ochoa, O., 2004. Transient heat transfer analysis of functionally graded materials using adaptive precise time integration and graded finite elements. Numerical Heat Transfer. Part B: Fundamentals 45 (2), 181–200.

Crawley, E.F., Luis, J.D., 1987. Use of piezoelectric actuators as elements of intelligent structures. AIAA Journal 25, 1373–1385.

Dong, S., Tong, L., 2001. Vibration control of plates using discretely distributed piezoelectric quasi-modal actuators/sensors. AIAA Journal 39, 1766–1772.

Feldman, E., Aboudi, J., 1997. Buckling analysis of functionally graded plates subjected to uniaxial loading. Composite Structures 38 (1), 29–36.

Gasik, M.M., 1998. Micromechanical modeling of functionally graded materials. Computational Materials Science 13 (1), 42–55.

Koizumi, M., 1993. Concept of FGM. Ceramic Transaction 34, 3–10.

Loy, C.T., Lam, K.Y., Reddy, J.N., 1999. Vibration of functionally graded cylindrical shells. International Journal of Mechanical Sciences 41 (3), 309–324.

Mallik, N., Ray, M.C., 2003. Effective coefficients of piezoelectric fiber reinforced composites. AIAA Journal 41 (4), 704–710.

Mian, A.M., Spencer, A.J.M., 1998. Exact solutions for functionally graded and laminated elastic materials. Journal of the Mechanics and Physics of Solids 46 (12), 2283–2295.

Miller, S.E., Hubbard, J.E., 1987. Observability of a Bernoulli-Euler beam using PVF_2 as a distributed sensor. MIT Draper Laboratory report, July 1, 1987.

Praveen, G.N., Reddy, J.N., 1998. Nonlinear transient thermoelastic analysis of functionally graded ceramic metal plates. International Journal of Solids and Structures 35 (33), 4457–4476.

Ray, M.C., Reddy, J.N., 2004. Optimal control of thin circular cylindrical shells using active constrained layer damping treatment. Smart Materials and Structures 13 (1), 64–72.

Ray, M.C., Bhattacharyya, R., Samanta, B., 1993. Exact solutions for static analysis of intelligent structures. AIAA Journal 31, 1684–1691.

Ray, M.C., 2003. Optimal control of laminated shells with piezoelectric sensor and actuator layers. AIAA Journal 41 (6), 1151–1157.

Ray, M.C., Sachade, H.M., accepted for publication. Exact solutions for the functionally graded plates integrated with a layer of piezoelectric fiber-reinforced composite. ASME Journal of Applied Mechanics.

Reddy, J.N., Cheng, Z.Q., 2001. Three-dimensional solutions of smart functionally graded plates. ASME Journal of Applied Mechanics 68 (3), 234–241.

Sankar, B.V., 2001. An elasticity solution for functionally graded beams. Composite Science and Technology 61 (5), 689–696.

Santare, M.H., Thamburaj, P., Gazonas, G.A., 2003. The use of graded finite elements in the study of elastic wave propagation in continuously nonhomogeneous materials. International Journal of Solids and Structures 40 (21), 5621–5634.

Shen, H.S., 2002. Nonlinear bending response of functionally graded plates subjected to transverse loads and in thermal environments. International Journal of Mechanical Sciences 44 (3), 561–584.

Stöbener, U., Gaul, L., 2000. Modal vibration control for PVDF coated plates. Journal of Intelligent Material Systems and Structures 11 (4), 283–293.

Suresh, S., Mortensen, A., 1998. Fundamentals of Functionally Graded Materials. Maney, London.

Teymur, M., Chitkara, N.R., Yohngjo, K., Aboudi, J., Pindera, M.J., Arnold, S.M., 1996. Thermoelastic theory for the response of materials functionally graded in two directions. 33 (7), pp. 931–966.

Vel, S.S., Batra, R.C., 2003. Three-dimensional analysis of transient thermal stresses in functionally graded plates. International Journal of Solids and Structures 40 (25), 7181–7196.

Wang, B.L., Han, J.C., Du, S.Y., 2000. Crack problems for Functionally Graded Materials under transient thermal loading. Journal of Thermal Stresses 23 (2), 143–168.

Woo, J., Meguid, S.A., 2001. Nonlinear analysis of functionally graded plates and shallow shells. International Journal of Solids and Structures 38 (42), 7409–7421.

Yang, J., Shen, H.S., 2001. Dynamic response of initially stressed functionally graded rectangular thin plates. Composite Structures 54 (4), 497–508.

Yang, J., Kitipornchi, S., Liew, K.M., 2003. Large amplitude vibration of thermo-electro-mechanically stressed FGM laminated plates. Computer Methods in Applied Mechanics and Engineering 192 (35), 3861–3885.

Yang, Y.Y., 2000. Time-dependent stress analysis in functionally graded materials. International Journal of Solids and Structures 37 (51), 7593–7608.